Boundary-Layer Effects on the Flowfield about Isolated Flow-Through Nacelles

William B. Compton III*
NASA Langley Research Center, Hampton, Virginia
and
John L. Whitesides†
George Washington University, NASA Langley Research Center, Hampton, Virginia

A numerical study has been made of boundary-layer effects on the flowfield about isolated flow-through nacelles. A viscous-inviscid interacting computational model for investigating the problem was constructed by coupling a three-dimensional explicit Euler solution procedure with a compressible, "lag-entrainment," integral boundary-layer solution technique. Solutions were obtained with the interacting model for long-duct turbofan engine nacelles at a freestream Mach number of 0.8 and an angle of attack of 0 deg. The physics of the interactions between the internal and external flows and the manner in which the boundary layer alters these interactions are analyzed. The computational results are compared to experimental data.

Introduction

TRANSPORT aircraft are being designed with more efficient high-bypass-ratio engines than in the past. When these large engines are combined with the airframe, complicated rotational flows can be generated, usually creating aerodynamic interference between the two systems. The interference can either reduce or increase the airplane's performance. Therefore, design engineers must increase their understanding of the aerodynamic interactions between the various components of the propulsion system and airframe well beyond the understanding that now exists. Both experimental and theoretical research is required.

Studies of this type using inviscid, irrotational computational methods, which range from panel techniques to solutions of the full transonic potential equation,[1-3] have proved to be very useful in the aircraft industry. Nevertheless, to conduct propulsion-integration research, engineers need techniques that adequately simulate the rotational flows. To address this need, a study was recently made of implicit and explicit computational solutions of the three-dimensional Euler equations for an isolated flow-through nacelle. The study, which preceded the present investigation, included three-dimensional flows with the nacelle at the angle of attack. The results are presented in Refs. 4 and 5. In general, the pressures predicted by both computational techniques agree well with the wind tunnel data on the external surface of the nacelle. However, for both procedures, large differences were observed between the inviscid computations and the wind tunnel data on the internal surface.

The present paper has been generated as a result of analyzing these discrepancies between the Euler computations and experiment. Since the Euler equations model compressibility and rotationality, but not viscous stresses, a preliminary assessment was made of the limitations imposed by the inviscid nature of the equations. To make the assessment, a viscous-inviscid interacting computational model was constructed by coupling the explicit three-dimensional Euler solution procedure with a two-dimensional strip boundary-layer solution procedure. The globally interacting technique included only weak boundary-layer interaction theory.

The investigations with the interacting model have yielded new insight into the mechanics of the interactions between the internal and external flows. While the viscous-inviscid interacting computational model is briefly described in this paper, emphasis is placed on the physics of the interactions between the internal and external flows and the manner in which the boundary layer alters these interactions.

Computational Procedure

Governing Flow Equations

For the initial inviscid study of the solution of the flowfield about a flow-through nacelle,[4-5] the three-dimensional Euler equations were chosen because they model both compressibility and rotationality. In order to simulate viscous effects for the present study, the explicit Euler solution procedure, described in Ref. 5, was coupled with a boundary-layer solution procedure. The resulting viscous-inviscid interacting computational model is based on a global iteration between the integration of the Euler equations and the boundary-layer equations.

Euler Equations

The Euler equations mathematically describe the physical laws governing the motion of an inviscid compressible fluid with variable entropy. In the present solution procedure, the three-dimensional time-dependent Euler equations are normalized and written in strong conservation form for a Cartesian coordinate system. If body forces are neglected, these time-dependent equations for mass, linear momentum, and energy can be expressed in vector notation as

$$\frac{\partial q}{\partial t}+\frac{\partial f}{\partial x}+\frac{\partial g}{\partial y}+\frac{\partial h}{\partial z}=0 \tag{1}$$

Presented as Paper 85-1623 at the AIAA 18th Fluid Dynamics and Plasmadynamics and Lasers Conference, Cincinnati, OH, July 16-18, 1985; received Nov. 1, 1985; revision received April 25, 1986.

*Aerospace Engineer, Propulsion Aerodynamics Branch, Transonic Aerodynamics Division. Member AIAA.
†Professor of Engineering and Applied Sciences, Joint Institute for Advancement of Flight Science. Associate Fellow AIAA.

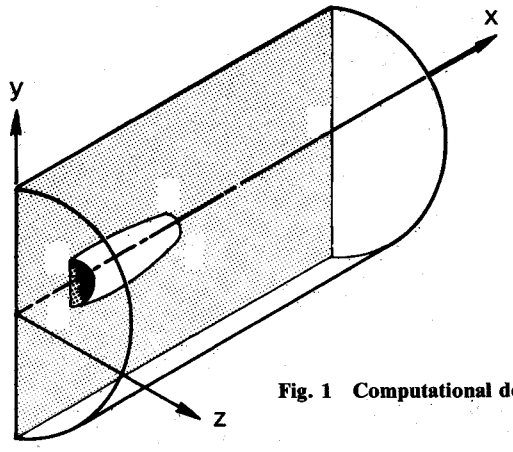

Fig. 1 Computational domain.

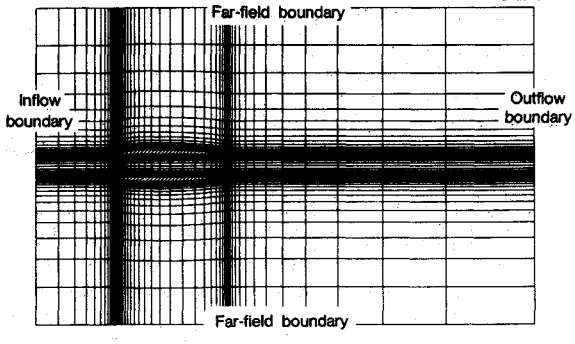

Fig. 2 Cross section of a typical three-dimensional grid.

where

$$q=\begin{Bmatrix}\rho\\ \rho u\\ \rho v\\ \rho w\\ \rho E\end{Bmatrix},\qquad f=\begin{Bmatrix}\rho u\\ \rho u^2+p\\ \rho uv\\ \rho uw\\ u(\rho E+p)\end{Bmatrix} \tag{2a}$$

$$g=\begin{Bmatrix}\rho v\\ \rho uv\\ \rho v^2+p\\ \rho vw\\ v(\rho E+p)\end{Bmatrix},\qquad h=\begin{Bmatrix}\rho w\\ \rho uw\\ \rho vw\\ \rho w^2+p\\ w(\rho E+p)\end{Bmatrix} \tag{2b}$$

In these equations, u, v, and w are velocities in the physical coordinate system (coordinates x,y,z), ρ the density, p the pressure, and E the total energy.

The equation of state,

$$p=\rho RT \tag{3}$$

where R is the gas constant and T the temperature, completes the system of equations.

Only solutions to steady flows are considered in this analysis. In this case, the total enthalpy does not vary throughout the flowfield of the flow-through nacelle. Hence, the energy equation, the fifth quantity of Eqs. (2) can be replaced by the condition of constant enthalpy. However, for propulsive flows, the enthalpy is generally not constant due to the jet exhaust. Therefore, to be consistent with the ultimate objective of eventually applying the computational model to propulsive flows with a high-energy exhaust, the full energy equation was solved along with the continuity and linear momentum equations.

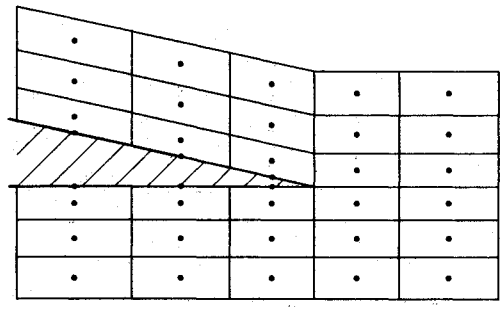

Fig. 3 Cross section of the trailing-edge region.

Boundary-Layer Equations

Since the objective of the present viscous-inviscid interacting research was to evaluate the viscous effects on the nacelle flowfield, a boundary-layer solution procedure that was well validated was desired for coupling with the Euler equations. Wind tunnel data indicate that the flow on the nacelle remains attached. Therefore, an integral technique that could be used in the direct mode was considered applicable.[6] Green's[7] compressible, two-dimensional axisymmetric, turbulent, "lag-entrainment" method solved in the direct mode was chosen because of its reliability.

The method involves the integration of three ordinary differential equations covering the momentum integral and entrainment equations, and the rate equation for the entrainment coefficient. These equations are

$$\frac{d\theta}{dx}=\left[\frac{RC_f}{2}-(H+2-M^2)R\frac{\theta}{U_e}\left(\frac{dU_e}{dx}\right)-\theta\frac{dR}{dx}\right]\left(\frac{1}{R}\right) \tag{4a}$$

$$\frac{d\bar{H}}{dx}=\left[\frac{dH}{dH_1}C_e-H_1\left(\frac{c_f}{2}-(H+1)\frac{\theta}{U_e}\frac{dU_e}{dx}\right)\right]\left(\frac{1}{\theta}\right) \tag{4b}$$

$$\frac{dC_e}{dx}=\left[\frac{F}{\theta}\frac{2.8}{H-H_1}\left((c_\tau)_{eq\infty}^{1/2}-\lambda c_\tau^{1/2}\right)+\left(\frac{\theta}{U_e}\frac{dU_e}{dx}\right)\right.$$
$$\left.-\frac{\theta}{U_e}\frac{dU_e}{dx}\left(1+0.075M^2\frac{(1+0.2M^2)}{(1+0.1M^2)}\right)\right] \tag{4c}$$

The momentum integral equation (4a) is obtained by integrating in the direction normal to the wall both the continuity and streamwise momentum equations and combining the results. The entrainment equation (4b) is obtained by integrating the continuity equation in the direction normal to the wall. The rate equation (4c) for the entrainment coefficient comes from a similar integration of the energy equation and represents explicitly the balance between the convection, production, diffusion, and dissipation of kinetic energy.

In Eqs. (4), θ is the momentum thickness, R the radius of the body, and C_e the entrainment coefficient. The terms H, $\bar{H}$, and H_1 are shape factors and F a function of the entrainment coefficient and the equilibrium skin-friction coefficient at zero

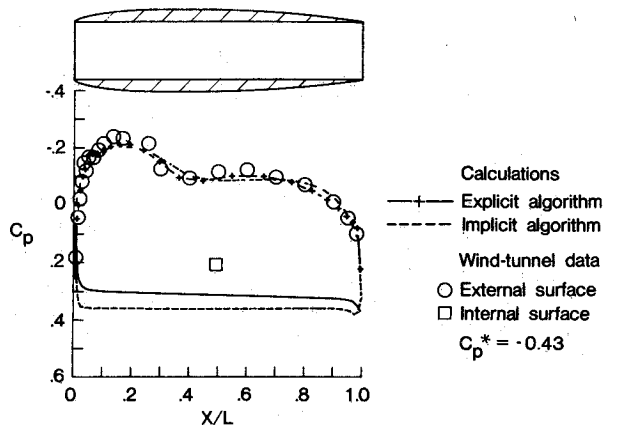

a) $M_\infty = 0.80$.

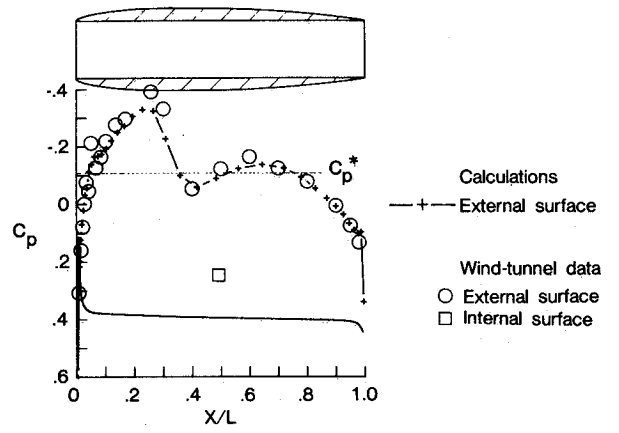

b) $M_\infty = 0.94$.

Fig. 4 Experimental and calculated pressures for the inviscid Euler equations ($\alpha = 0.0$ deg).

pressure gradient. The term C_f is the skin-friction coefficient and C_τ the shearing-stress coefficient.

These boundary-layer equations are integrated along the body surface in a strip fashion in each azimuthal plane by using a variable order, variable interval Adams method. The method is part of the Langley Cyber 200 mathematical library[8] and is recommended for sets of stiff first-order ordinary differential equations.

Computational Domain and Grid System

A sketch of the nacelle and the three-dimensional domain in which the computations were carried out is presented in Fig. 1. Three dimensionality is produced by rotating the vertical cross section about the axis of the nacelle, thus generating a cylindrical domain. To minimize computer run time and storage requirements, symmetry is assumed about the vertical plane and only one-half of the cylindrical domain is computed.

The grid system constructed for the discretized solution procedure is body fitted (the grid lines coincide with the nacelle surface and other boundaries) in order to facilitate implementation of the boundary conditions. It is a sheared, H-type computational grid. Figure 2 presents a vertical cross section of the grid in the physical space, again illustrating the nacelle geometry and the various boundaries. The grid mesh in the circumferential direction is generated by rotating the vertical cross section about the axis of the nacelle. The spacing between the mesh lines is geometrically stretched away from the nacelle, with the lines being clustered near the nacelle surface and near the leading and trailing edges.

The main computations were made with 58 axial grid planes (30 along the nacelle), 29 grid planes in the radial direction,

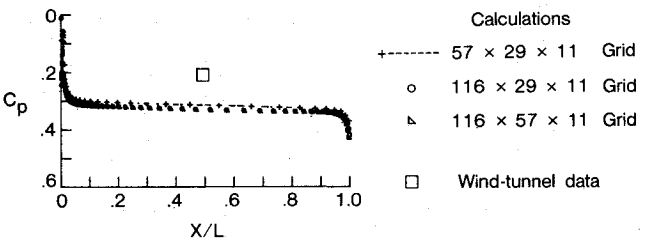

Fig. 5 Effect of grid refinement on the internal pressures ($\alpha = 0$ deg, $M_\infty = 0.80$).

and 11 in the circumferential direction. A brief study was also made with two refined grids. The number of grid planes in the axial, radial, and circumferential directions for the two refined grids were, respectively, 116, 29, and 11 and 116, 57, and 11.

Nacelle Configuration

Solutions were obtained for flow-through nacelles with three different ratios of the length to maximum diameter. One nacelle has a length to maximum diameter of 3.5, which would be typical of a mixed-flow (long-duct) version of a medium-bypass-ratio engine nacelle. Another nacelle has a length to maximum diameter of 2.5, which is similar to high-bypass-ratio, mixed-flow nacelles being proposed for future use on commercial transport aircraft. The third nacelle is included as a limiting case. Its ratio of length to maximum diameter is 1.28, which for a long-duct nacelle represents a bypass ratio much higher than the engines currently being used on transport aircraft.

The external surface of each nacelle consists of a NACA 1-70-100 inlet, a cylindrical section, and a circular arc afterbody. The internal ducts of the nacelles are cylindrical.

Inviscid Numerical Method

Algorithm

To solve the three-dimensional Euler equations, an explicit finite volume procedure employing a fourth-order Runge-Kutta numerical algorithm was used. The finite volume formulation allows the equations to be solved in the physical space and eliminates the necessity of a transformation. The algorithm has been applied to both two- and three-dimensional problems and appears to give accurate and stable solutions in both cases.[9-11] The explicit procedure was adapted to the nacelle problem from an existing computer code written by Jameson and Baker[11] by changing the logic of the code to allow for both internal and external nacelle surfaces on an H-type grid. Essentially, the explicit interior point algorithm and boundary treatments were modified and inserted into the overall framework of an implicit computer code developed by Compton and Whitesides[4] specifically for the nacelle problem.

Boundary Conditions

The treatment of the inflow, outflow, and far-field boundaries is based on the Riemann invariants for a one-dimensional flow normal to the boundary.[11] The Riemann invariants originating from outside and inside the computational domain are combined to yield the velocity normal to the boundary and the speed of sound at the boundary. At an inflow boundary, a function of the entropy and the tangential velocities are additionally specified by setting them equal to their freestream values. This combination completely defines the flow conditions. The far-field boundary is treated as an inflow boundary.

At an outflow boundary, the Riemann invariants again yield the speed of sound and the normal velocity. The tangential velocities and the function of the entropy are obtained

from within the computational domain by using zero-order extrapolation.

The boundary condition for a solid body in inviscid flow is that the flow is tangent to the body surface (i.e., no mass flux normal to the surface). Furthermore, for solving the Euler equations using a finite volume formulation, the pressure is the only surface boundary property that appears explicity. The relationship used in Ref. 11 for determining the surface pressure is the normal momentum equation, or,

$$g^{m2}\frac{\partial p}{\partial \zeta^m}=\rho\left[W^1\left(u^j\frac{\partial n_j}{\partial \zeta^1}\right)+W^3\left(u^j\frac{\partial n_j}{\partial \zeta^3}\right)\right] \tag{5}$$

where n is the unit normal to the surface and

$$u^j=\frac{dx^j}{dt},\quad W^1=\frac{d\zeta^1}{dt},\quad W^3=\frac{d\zeta^3}{dt},\quad g^{m2}=\frac{\partial \zeta^m}{\partial x^\ell}\frac{\partial \zeta^2}{\partial x^\ell} \tag{6}$$

The terms ζ^j are curvilinear coordinates that coincide with the grid. Double indices indicate summation. Using Eq. (5), the gradient can be evaluated and the pressure extrapolated to the body.

Directly treating the nacelle's trailing edge (such as applying a "Kutta-like" condition) can strongly affect the solution.[5] The finite volume Euler formulation used in this investigation has the advantage in that it does not require a specific boundary treatment of the leading or trailing edges of the nacelle. Hence, none was applied. The surface pressures at the midcell points and the dependent flow variables at the cell centers (see Fig. 3) define completely the information needed in this region to advance the numerical integration.

Also, it should be emphasized that the computational domain extended continuously from well in front of the nacelle, through its duct, and beyond the rear of the nacelle. There were no boundaries and, therefore, no boundary conditions at the inlet and exit planes of the nacelle. As a result, the internal mass flow developed naturally, being determined only by the nacelle geometry and the freestream conditions.

The explicit finite volume algorithm is thoroughly described in Refs. 9–11 and its application to the nacelle problem, including boundary conditions, in Ref. 5.

Viscous-Inviscid Interacting Theory

Matching Conditions

The globally viscous-inviscid interacting technique depends upon a coupling of the inviscid Euler equations and the boundary-layer equations through conventional transpiration boundary conditions. As pointed out by Thomas,[12] for the inviscid Euler solution to simulate a solution with viscous effects, it must match the viscous solution in that part of the flowfield where the inviscid and viscous equations both describe the flow accurately.

In matching the viscous and inviscid solutions in two dimensions, Thomas[12] follows the example of Johnston and Sochol.[13] They integrate the Navier-Stokes and Euler equations from the wall, in the direction normal to the wall, to the point where both sets of equations describe the flow accurately. By matching the two solutions at this point, an equation for the Euler vector normal to the wall is obtained as follows:

$$g_w=G_w+\frac{\partial}{\partial x}\int_0^h (f-F)dy \tag{7}$$

where f and g represent the vectors in the set of Euler equations and F and G the vectors in the Navier-Stokes equations. The subscript w indicates wall values. The Euler vector g_w is identically the vector of the transpiration boundary conditions that are imposed at the body surface and in the wake of the body to enforce the boundary-layer effects.

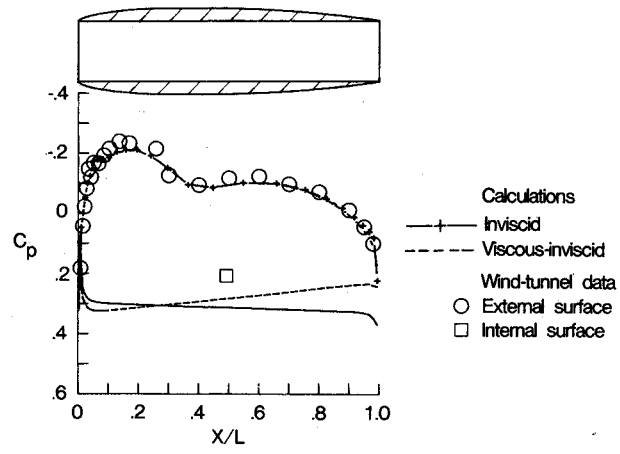

a) Medium-bypass nacelle, $L/D_{max}=3.5$.

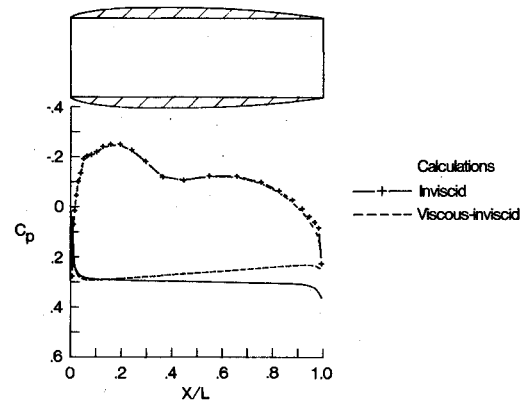

b) High-bypass nacelle, $L/D_{max}=2.5$.

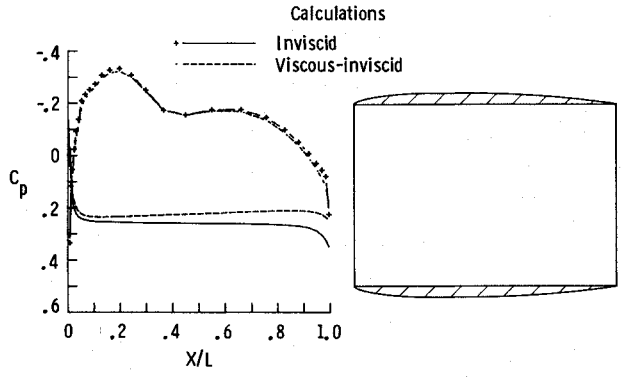

c) Very-high-bypass nacelle, $L/D_{max}=1.28$.

Fig. 6 Effect of viscous-inviscid interaction on the nacelle pressures ($M_\infty=0.80$, $\alpha=0.0$ deg, $Re=4.9\times10^6$).

Using the continuity equation as an example, the equivalent inviscid boundary condition at the wall necessary to match the inviscid and viscous solutions is

$$(\rho v)_w=\frac{d}{dx}[(\rho u)_w\delta^*] \tag{8}$$

where δ^* is the boundary-layer displacement thickness. Note that Johnston and Sochol use the inviscid wall values in determining the mass flux term on the right-hand side of Eq. (8). This is the same equation as the one presented by Lock.[14] It states that the mass flow normal to the wall in the equivalent inviscid flow is equal to the streamwise rate of change of the mass flow deficit produced by the boundary layer.

The viscous-inviscid interaction technique presented here uses a three-dimensional adaptation of the two-dimensional matching procedure. By performing a mass balance for the flow between two axial stations and the wall and the edge of the boundary layer, it can be shown that the axisymmetric equivalent of Eq. (8) is

$$(\rho V)_w = \frac{1}{2r}\frac{\mathrm{d}}{\mathrm{d}x}[(\rho u)_w(2r\delta^* + \delta^{*2})] \tag{9}$$

where V is the velocity vector normal to the surface. For the three-dimensional adaptation, V is divided into components v and w in the vertical and horizontal directions, respectively. Due to the relatively small boat-tail angles of the nacelle, the axial component is neglected. Using these quantities and the inviscid values of the tangent velocity u_w and pressure p_w at the surface, the equivalent inviscid vectors g_w and h_w can be evaluated at the surface of the nacelle, where

$$g_w = \begin{Bmatrix} \rho v \\ \rho uv \\ \rho v^2 + p \\ \rho vw \\ v(\rho E + p) \end{Bmatrix}_w, \qquad h_w = \begin{Bmatrix} \rho w \\ \rho uw \\ \rho vw \\ \rho w^2 + p \\ w(\rho E + p) \end{Bmatrix}_w \tag{10}$$

Surface Pressure Equation

Allowing flow across the solid nacelle boundary introduces the following extra term in the surface pressure equation [Eq. (5)]:

$$-\rho\left[W^1\frac{\partial}{\partial\xi^1}(n_j u^j) + W^3\frac{\partial}{\partial\xi^3}(n_j u^j)\right]$$

This term is appended to the right-hand side of Eq. (5).

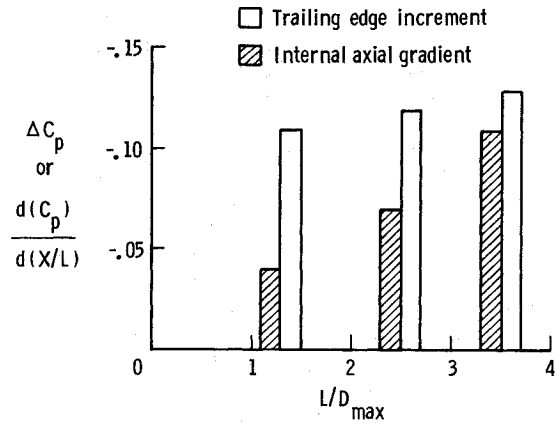

Fig. 7 Summary of viscous effects ($M_\infty = 0.80$, $\alpha = 0.0$ deg, $Re = 4.9 \times 10^6$).

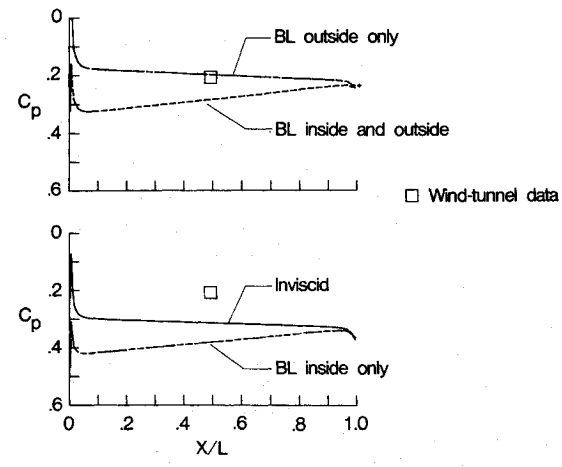

Fig. 8 Viscous effects on the internal nacelle pressures ($M_\infty = 0.80$, $\alpha = 0.0$ deg, $Re = 4.9 \times 10^6$).

Application of the Viscous-Inviscid Interaction Technique

The transpiration boundary conditions presented in Eq. (10) are applied on both the external and internal nacelle surfaces and also in the wake of the nacelle. In this discussion, "wake" refers to the wake of the boundary layer. It needs to be considered only for the application of the transpiration boundary conditions. Consideration of an inviscid wake in solving the Euler equations was not necessary.

The transpiration boundary conditions in the wake are imposed along an imaginary shell of constant radius, starting at the nacelle trailing edge and extending approximately one-half of the nacelle cord downstream. At this axial location, the wake boundary condition had decayed to a very low value. Imposing the wake transpiration boundary conditions at the imaginary shell instead of the trailing-edge streamline is similar to making a slender-body approximation in the wake. As long as the trailing-edge streamline remains close to the shell, any errors produced by the approximation should be of second order. However, when numerically integrating the Euler equations, fluxes were allowed to flow freely through the imaginary shell and a pressure balance was maintained across it.

In the overall global iteration between the Euler and boundary-layer solutions, the boundary-layer equations are solved every 100 time steps of the Euler integration process, using the current values of the viscous-inviscid solution. The transpiration boundary conditions are then updated using the new boundary-layer solution and held constant until the next global iteration. After 10 overall global iterations, the solutions essentially ceased to change.

The transpiration boundary conditions described in the preceding sections account for the displacement effects of the boundary layer. They do not account for wake curvature effects, which are theoretically important, but in practice usually smaller in magnitude.[15] They also do not account for such strong interaction effects as the interaction between the boundary layer and a strong shock wave that results in a breakdown of the usual boundary-layer approximations.[15]

Results

Relationship Between the Inviscid Computations and Experiment

Preceding Results

Recently, two different computational procedures for solving the three-dimensional Euler equations were evaluated.[4,5] The evaluation was conducted specifically for an isolated flow-through nacelle configuration. The first computational procedure employed an alternating-direction-implicit (ADI) numerical algorithm and the second procedure employed an explicit fourth-order Runge-Kutta numerical algorithm. The techniques were used to compute the flowfield for a long-duct turbofan engine nacelle at freestream Mach numbers of 0.80 and 0.94 and angles of attack of 0 and 4 deg.

The results of these inviscid calculations are presented in Refs. 4 and 5. In general, the pressures predicted by both computational procedures agree very well with the wind tunnel data on the external surface of the nacelle. The implicit technique utilized a Beam and Warming numerical algorithm, which made it weakly unstable since the problem is formulated in three dimensions. However, the instability required a very

large number of time steps to develop. For a moderate number of time steps (~1000), it yielded reasonably accurate results for engineering purposes.[4,5] The explicit technique proved to be stable and predicted pressures that are in even better agreement with experiment on the external surface of the nacelle than those calculated by the implicit numerical procedure.

In contrast to the calculations for the external surface, large differences were observed between the inviscid computations and the wind tunnel data on the internal surface of the nacelle. Figure 4 (which is taken from Ref. 5) presents a sample of the calculations made with the implicit and explicit codes at a freestream Mach number of 0.80 and 0.94 and an angle of attack of 0.0 deg. Wind tunnel data of Re and Reddrew[16] are included in the figure. It shows that the calculated internal pressures are much more positive (further from freestream) than the wind tunnel data. In a similar observation, Miranda[17] indicates that the inviscid potential solutions of similar configurations frequently give good solutions for the external flow, but yield the incorrect internal mass flow ratio.

It should be re-emphasized that there were no boundary conditions at the inlet and exit planes of the nacelle. Hence, the internal mass flow developed naturally. In inlet studies, the experimental mass flow is usually controlled and the boundary conditions at the duct exit determine the computed mass flow. As a result of matching the computed and experimental mass flows, good correlation between internal computations and experiment is usually obtained for inlets.[18-20] In the current flow-through nacelle study, the computed and experimental mass flows were not matched since each internal flow developed naturally.

Effect of Grid Refinement

The effect of grid clustering in the vicinity of the trailing edge was investigated by obtaining inviscid Euler solutions with two refined grids. In the vicinity of the trailing edge, the axial grid point clusterings of the two refined grids were three times as dense as the standard mesh. In addition to the axial refinement, one of the improved grids had a radial density twice the standard.

Solutions with the two refined coordinate systems show no better internal agreement with the data than the standard solution, as shown in Fig. 5. In fact, a closer mesh spacing in the axial direction even gives a very slight increase in the discrepancy between the data and the computations. There is almost no effect of additionally refining the mesh in the radial direction. Although this grid refinement study is brief, it indicates that grid spacing is not the source of the large disagreement between the inviscid Euler calculations and the data inside the nacelle's duct.

Viscous-Inviscid Interacting Computational Results

The Euler equations model inviscid rotationality and compressibility, which makes it unlikely that the incorrect representation of these two phenomena generates the discrepancy between the calculations and experiment. Also, as just described, grid clustering does not account for the large differences. The possibility that the Euler equations are giving the correct relationship between the inviscid solution and the data led to the present study. In it, boundary-layer effects on the interactions between the internal and external flows are examined.

The viscous-inviscid interacting computational model described earlier (the explicit Euler procedure coupled with the integral "lag-entrainment" boundary-layer integration technique) was used to conduct the investigation. Calculations were made at a freestream Mach number of 0.80 and an angle of attack of 0.0 deg. All viscous-inviscid interacting computations were made for a turbulent boundary layer and a Reynolds number of 4.9×10^6 based on the length of the nacelles. The Reynolds number for the computations was chosen to match the experimental value.

Overall Viscous Effects

The overall result of combining the boundary layer effects with the inviscid Euler solution is illustrated in Fig. 6. Figure 6a presents the results for the standard nacelle. The standard nacelle has dimensions typical of a mixed-flow version of a nacelle for a medium-bypass-ratio engine. Figure 6b presents the results for a high-bypass mixed-flow nacelle with dimensions similar to those being proposed for future commercial transport aircraft. The calculations for the very-high-bypass nacelle are shown in Fig. 6c.

Figure 6 presents the viscous-inviscid interacting solutions as well as the inviscid solutions. It illustrates that the viscous effects significantly change the internal pressures. The effects on the external surfaces are small. Specifically, the boundary layer significantly decreases the exit pressures and produces sizable axial pressure gradients in the nacelle ducts.

For the medium-bypass nacelle, for which there is experimental data, the net effect improves the correlation between the computed internal pressures and the data. See Fig. 6a. However, they do not match perfectly. It is believed that the data point is valid even though the correct internal pressure level and gradient cannot be definitely established without additional experimental data. As pointed out previously, this interacting procedure compensates for the boundary layer and wake thickness, but not the curvature effects. Melnik[15] indicates that wake curvature, while not being as important as wake thickness, also has a similar effect. Hence, if allowance were made for boundary layer and wake curvature in the present calculations, the computations should match the internal pressure datum even better.

The primary result of the correlation between the internal calculations and experiment is that there is better agreement with data when the boundary-layer effects are included. This result lends confidence that the prediction of the effects of viscosity is at least qualitatively correct.

Figure 7 presents a summary of the viscous effects. It presents the internal axial pressure gradient as a function of the ratio of the length of each nacelle to its maximum diameter. The figure also includes the change in the trailing-edge, or exit, pressure between the inviscid and the viscous-inviscid solutions. Figure 7 illustrates that, as the diameter of the nacelle gets larger relative to its length, the boundary layer produces a significantly smaller internal pressure gradient. The decrease in the exit pressure produced by the boundary-layer changes less rapidly as the nacelle's diameter varies.

External and Internal Boundary Layers

An attempt was made to determine the relative importance of the external and internal boundary layers on the solution. Therefore, in addition to the inviscid and the complete viscous-inviscid interacting solutions, interacting computations were made with the the boundary layer and wake originating only from the external surface of the nacelle. Similar computations were also made with the boundary layer and wake originating only from the internal surface. All of these calculations were made for the standard medium-bypass nacelle with a length-to-maximum-diameter ratio of 3.5.

First, the influence of the boundary layer and wake originating from only the external surface of the nacelle is considered. The top part of Fig. 8 contains the pressure distributions for the complete viscous-inviscid interacting solution and for the solution that includes the viscous effects produced by only the external nacelle surface. The common factor between the curves is that each includes the viscous effects originating from the external surface of the nacelle. Even though there are differences in the pressure gradients between the two calculations, the exit pressures in both cases are the same.

The viscous effects due to the external nacelle surface are absent in the bottom part of Fig. 8. It presents the inviscid solution and the interacting solution with only the internal boundary layer and wake. Again the pressure gradients are different, but the exit pressures of both curves are equal. The

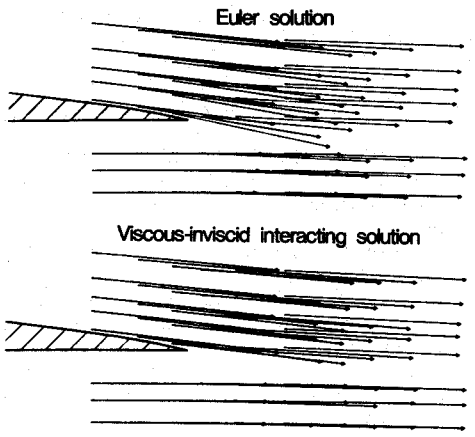

Fig. 9 Viscous effects on the velocities in the vicinity of the trailing edge ($M_\infty = 0.80$, $\alpha = 0.0$ deg, $Re = 4.9 \times 10^6$).

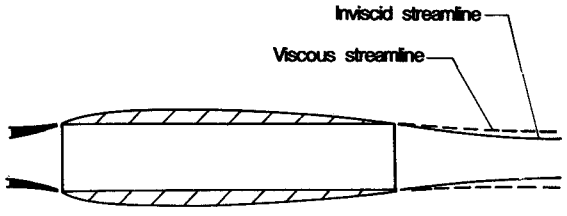

Fig. 10 Inviscid and viscous streamlines.

two comparisons show that the external boundary layer and its wake in combination with the inviscid flow determine the exit pressure and hence the overall pressure level of the internal flow. The internal boundary layer has very little effect on the exit pressure.

An examination of both sets of pressure distributions also illustrates that the internal boundary layer produces the pressure gradient in the nacelle duct. In addition, it shows that the gradient is essentially unaffected by the boundary layer on the outside surface. One-dimensional axisymmetric calculations demonstrate that the gradient is the result of the change in the effective duct area due to the growth of the internal boundary layer. For example, the one-dimensional calculation yielded a pressure coefficient gradient of 0.13 vs the gradient of 0.11 given by the present viscous-inviscid calculation.

The calculations for the three nacelles show that the magnitude of these results is configuration dependent, as can be seen in Fig. 7. For example, in the limit as the ratio of the maximum diameter to length of the nacelle becomes very large, the internal boundary layer will include a negligible percentage of the effective duct area. Hence, the internal axial pressure gradient will become negligibly small. Also, in this instance, one would expect the decrease in the trailing-edge pressure produced by the boundary layer to become a localized effect.

Decambering Effect

A more complete understanding of the mechanism by which the boundary layer produces these results can be gained by considering Fig. 9. It shows the velocity vectors in the vicinity of the trailing edge for the inviscid solution and the corresponding vectors for the interacting solution. Comparing the two velocity vector plots illustrates the difference in the basic nature of the two solutions; the inviscid solution possesses a greater inward radial component of the flow, which suggests a greater circulation.

The external viscous effects produce a change in the stream velocities that is similar to a change that would be produced by decambering the nacelle. The analysis presented above strongly indicates that the external boundary layer effectively decambers the nacelle and alters the overall flow pattern by redirecting the streamlines closer to the freestream direction. A sketch of the inviscid and viscous streamlines is presented in Fig. 10. The compression on the external surface of the nacelle is thus weakened, yielding a less positive exit pressure and a less positive internal pressure level. The end result is an increase in mass flow through the nacelle's duct. Hence, if simulation of the correct mass flow through the nacelle duct is important in analyzing a fluid flow problem, then viscous effects on both the internal and external surfaces must be included in the computational model.

Conclusions

A numerical study has been made of the boundary-layer effects on the flowfield about isolated flow-through nacelles. A viscous-inviscid interacting computational model for investigating the problem was constructed by coupling a three-dimensional Euler solution procedure with a compressible, "lag-entrainment" integral boundary-layer solution technique. The procedure for integrating the three-dimensional Euler equations employed an explicit fourth-order Runge-Kutta numerical algorithm and a finite volume formulation. The resulting viscous-inviscid interacting computational model is based on a global iteration between the integration of the Euler equations and the boundary-layer equations. The interacting model was used to investigate large differences previously observed between inviscid three-dimensional Euler computations and wind tunnel data on the internal surface of a flow-through nacelle. These investigations were conducted for long-duct turbofan engine nacelles at a freestream Mach number 0.80 and at an angle of attack of 0 deg.

For predicting the pressures on the external surface of the nacelle, viscous effects were relatively unimportant.

The numerical experiments show that, for predicting the flow inside the nacelle's duct, viscous effects are extremely important and that both the external and internal boundary layers and wakes must be simulated. The external boundary layer and its associated wake change the overall pattern of the inviscid flow. By displacing the streamlines away from the external surface of the nacelle, they effectively decamber the nacelle and thus weaken the compression at its trailing edge. This gives a less positive exit pressure and, hence, a less positive overall internal static pressure level. The reduced static pressure level, in turn, increases the mass flow through the nacelle. The internal boundary layer creates an axial pressure gradient in the duct, but essentially does not affect the overall pressure level. Hence, if simulating the correct mass flow through the nacelle's duct is important, then viscous effects on both the internal and external surfaces must be included in the computational model.

References

[1]Hess, J. L., "Calculation of Potential Flow About Arbitrary Three-Dimensional Lifting Bodies," McDonnell Douglas, Rept. MDC J5679-01, Oct. 1972.

[2]Boppe, C. W. and Stern, M. A., "Simulated Transonic Flows for Aircraft With Nacelles, Pylons, and Winglets," AIAA Paper 80-0130, Jan. 1980.

[3]Reyhner, T. A., "Computation of Transonic Potential Flow About Three-Dimensional Inlets, Ducts, and Bodies," NASA 351A, March 1982.

[4]Compton, W. B. III and Whitesides, J. L., "Three-Dimensional Euler Solutions for Long-Duct Nacelles," AIAA Paper 83-0089, Jan. 1983.

[5]Compton, W. B. III, "On the Solution of the Three-Dimensional Flowfield About a Flow-Through Nacelle," D.Sc. Dissertation, George Washington University, Washington, DC, May 1985.

[6]Anderson, D. A., Tannehill, J. C., and Pletcher, R. H., *Computational Fluid Mechanics and Heat Transfer*, Hemisphere Publishing Corp., New York, 1984, pp. 329-363.

[7]Green, J. E., Weeks, D. J., and Brooman, J. W. F., "Prediction of Turbulent Boundary Layers and Wakes in Compressible Flow by a

Lag-Entrainment Method," Royal Aircraft Establishment, Tech. Rept. 72231, Jan. 1973.

[8]"Cyber 200 Mathematical Library," Central Scientific Computing Document S-3, NASA Langley Research Center, Sec. VD2.1, Oct. 1984.

[9]Schmidt, W., Jameson, A., and Whitfield, D., "Finite Volume Solution for the Euler Equation for Transonic Flow Over Airfoils and Wings Including Viscous Effects," *Journal of Aircraft*, Vol. 20, Feb. 1983, pp. 127-133.

[10]Jameson, A., Schmidt, W., and Turkel, E., "Numerical Solutions or the Euler Equations by Finite Volume Methods Using Runge-Kutta Time-Stepping Schemes," AIAA Paper 81-1259, June 1981.

[11]Jameson, A. and Baker, T. J., "Solution of the Euler Equations for Complex Configurations," AIAA Paper 83-1929, June 1983.

[12]Thomas, J. L., "Transonic Viscous-Inviscid Interaction Using Euler and Inverse Boundary-Layer Equations," Ph.D. Dissertation, Mississippi State University, State College, Dec. 1983.

[13]Johnston, W. and Sochol, P., "A Viscous-Inviscid Interative Compressor Calculation," AIAA Paper 89-1140, July 1978.

[14]Lock, R. C., "A Review of Methods for Predicting Viscous Effects on Aerofoils and Wings at Transonic Speeds," AGARD CP 291, Paper 2, Sept.-Oct. 1980.

[15]Melnik, R. E., "Turbulent Interactions on Airfoils at Transonic Speeds—Recent Developments," AGARD CP 291, Paper 10, Sept.-Oct. 1980.

[16]Re, R. J. and Peddrew, K. H., "Tabulations of Static Pressure Coefficients on the Surface of Three Pylon-Mounted Axisymmetric Flow-Through Nacelles at Mach Numbers from 0.40 to 0.98," NASA 84540, Sept. 1982.

[17]Miranda, L., Private communication, Lockheed California Co. Burbank, CA, Sept. 1984.

[18]Crook, J. L., Nelson, D. P., Wiley, R. H., and Presz, W. M., "Isolated Nacelle Performance-Measurement and Simulation," AIAA Paper 82-0134, Jan. 1982.

[19]Golden, D. P., Barber, T. J., and Chin, W. C., "An Axisymmetric Nacelle and Turboprop Inlet Analysis with Flow-Through and Power Simulation Capabilities," AIAA Paper 82-0256, Jan. 1982.

[20]Chen, H. C., Yu, N. J., Rubbert, P. E., and Jameson, A., "Flow Simulations for General Nacelle Configurations Using Euler Equations," AIAA Paper 83-0539, Jan. 1983.